A multiscale theory for spreading and migration of adhesion-reinforced mesenchymal cells

Wenya Shu[1,2] and C. Nadir Kaplan[1,2]*

[1]Department of Physics,

Virginia Polytechnic Institute and State University, Blacksburg, VA 24061, USA.

[2]Center for Soft Matter and Biological Physics,

Virginia Polytechnic Institute and State University, Blacksburg, VA 24061, USA.

* To whom correspondence should be addressed: nadirkaplan@vt.edu

Abstract

We present a chemomechanical whole-cell theory for the spreading and migration dynamics of mesenchymal cells that can actively reinforce their adhesion to an underlying viscoelastic substrate as a function of its stiffness. Our multiscale model couples the adhesion reinforcement effect at the subcellular scale with the nonlinear mechanics of the nucleus-cytoskeletal network complex at the cellular scale to explain the concurrent monotonic area-stiffness and non-monotonic speed-stiffness relationships observed in experiments: We consider that large cell spreading on stiff substrates flattens the nucleus, increasing the viscous drag force on it. The resulting force balance dictates a reduction in the migration speed on stiff substrates. We also reproduce the experimental influence of the substrate viscosity on the cell spreading area and migration speed by elucidating how the viscosity may either maintain adhesion reinforcement or prevent it depending on the substrate stiffness. Additionally, our model captures the experimental directed migration behavior of the adhesion-reinforced cells along a stiffness gradient, known as durotaxis. We further demonstrate that, depending on where a simulated cell starts on a substrate with a viscosity gradient, it may migrate towards the more viscous region (viscotaxis) or in the opposite direction (anti-viscotaxis), moving towards an optimal viscosity in either case. Overall, our theory explains the intertwined mechanics of the cell spreading, migration speed and direction in the presence of the molecular adhesion reinforcement mechanism.

Author summary

There is a growing recognition that cells can actively sense both the elastic stiffness and viscosity of the extracellular matrix (ECM). Therefore, understanding the intricate relationship between the matrix properties and cell responses is crucial for gaining insights into various biological processes and tissue engineering. Here we present a multiscale chemomechanical theory for the regulation of cell spreading, migration speed and direction in the presence of adhesion reinforcement triggered on stiff substrates. Our theory successfully captures the monotonic area-rigidity relationship observed in experiments. Since we take into account the nucleus flattening and alteration of the cytoplasmic viscosity due to large cell spreading at high stiffness, our model yields an increased nucleus drag force and in turn a reduced migration speed on stiff substrates. That way, our model reproduces the experimental nonmonotonic speed-rigidity relationship. We also investigate the effect of viscosity on cell spreading and migration speed both on soft and stiff substrates. Our results uncover how directed cell migration is influenced by the viscosity gradients that prompt the cells to move towards regions with optimal relaxation dynamics. Altogether, our multiscale model elucidates the distinct responses of cell spreading and migration to the ECM stiffness and viscosity, offering insights for the experimental design and biomaterial optimization.

INTRODUCTION

Cell motion plays a crucial role in various biological processes ranging from tissue formation to metastasis. The mechanical properties of the extracellular matrix (ECM) are critical environmental cues that orchestrate the spreading and migration of adherent (mesenchymal) cells [1, 2, 3, 4, 5, 6, 7, 8]. Focal adhesion (FA) sites play a key role in cell mechanosensitivity by mediating the chemical and mechanical interactions between the cell and ECM. The FA dynamics can directly impact the chemically driven localized protrusions and contractions across the cell, governed by the tightly coupled spatiotemporal distributions of the proteins, such as the Rho GTPases, ROCK, or CDC42, which influence the migration dynamics [9, 10, 11, 12, 13, 14]. Thus, a rigorous mathematical description of cell migration must include accurate modeling of the adhesion forces at different FA sites and their coupling with the cytoskeletal dynamics driven by the intracellular signaling pathways.

Although some cells such as the U-251MG glioblastoma cells exhibit a biphasic dependence of the trac-

tion force on the rigidity of the underlying matrix [15, 16], which can be explained by the classical motor-clutch theory [17, 18], many other systems, such as endothelial cells and fibroblasts, display a monotonic rigidity-force relationship [19, 20]. This behavior is attributed to active adhesion reinforcement triggered by the unfolding of the talin molecules that leads to the vinculin binding and in turn to an increased integrin density at an FA site [21, 22]. While an augmented motor-clutch theory with adhesion reinforcement successfully captures the monotonic increase of the traction force with the matrix stiffness [23], it cannot explain the non-monotonic dependence of the migration speed on the ECM rigidity measured in the experiments [5, 6, 7, 8]. This suggests that the mutual dynamics of the many FA sites across the cell along with the cytoskeletal dynamics must be considered to relate the migration speed to the traction forces and in turn to the matrix rigidity, rather than at a single FA site. To reproduce the cell migration dynamics as a coordinated sequence of peripheral protrusion and contractions [24, 4, 25], whole-cell level formulations with multiple FA sites have been developed, including our recent theory that integrates the chemomechanical coupling between the Rho GTPase concentrations, the FA sites, the cytoskeletal network and the nucleus dynamics [26, 27, 28]. However, none of these studies have incorporated the adhesion reinforcement mechanism into the whole-cell dynamics. Importantly, we anticipate that a mere addition of the adhesion reinforcement effect to the whole-cell-scale model would still lead to a monotonic rigidity-speed relationship, implying further subtleties associated with the collective intracellular dynamics under adhesion reinforcement.

Here we generalize our multiscale theory in Ref. [28] to elucidate the spreading and migration dynamics of adhesion-reinforced cells on viscoelastic substrates, overcoming the limitations of our previous model without adhesion reinforcement. Our model demonstrates how the nonlinear mechanics of the nucleus–cytoskeletal network complex must play a critical role in the experimental spreading and biphasic stiffness-speed profiles: Large cell spreading on stiff substrates induced by the augmented local traction forces due to adhesion reinforcement, an effect accurately captured by our model, deforms the nucleus [29] and increases both the cytoplasmic viscosity and cytoskeletal stiffness [8, 30, 31, 32]. Consequently, the drag force on the nucleus increases, making it harder for the cell to translocate the nucleus on stiff substrates, as evidenced by a theoretical non-monotonic stiffness-speed relationship in quantitative agreement with experiments. By using the standard linear solid model for the substrate viscoelasticity, we also investigate the effect of the substrate stress relaxation on cell migration across a broad stiffness range, which is experimentally well documented [33, 34, 35, 23]. We show that, on a substrate with high elastic stiffness, fast stress relaxation (low viscosity) may preempt the effect of adhesion reinforcement whereas slow relaxation (high

viscosity) may promote it. That way, our model quantitatively reproduces the experimental spreading area and migration speed profiles of the HT-1080 human fibrosarcoma cells [27]. Furthermore, we demonstrate that adhesion-reinforced cells persistently move up the stiffness gradients, i.e., durotaxis [36, 37, 38], in good agreement with the experimental migration patterns of the MDA-MB-231 cells [16]. We also reveal the effect of the viscosity gradients on directed migration, a.k.a. viscotaxis, which sheds light on the migration of human mesenchymal stem cells from high to low loss moduli on collagen coated polyacrylamide gels [39].

Our theory provides a rigorous understanding of how the nucleus drag as a function of cell spreading gives rise to the experimentally observed complex migration dynamics, in contrast with the previous phenomenological treatments that assumed a direct functional relationship between the drag force, the traction force, and substrate stiffness [40, 41]. Furthermore, because our model takes into account additional intracellular components beyond just the FA sites, it provides a plausible mechanism for the emergent nonuniform stiffness-speed relation that complements the cell model which relates cell speed only to the resultant traction force from the collective adhesion-reinforced FA dynamics [42].

METHODS

Mesenchymal migration entails the spatiotemporal coordination of front protrusion driven by actin polymerization and focal adhesion (FA) followed by rear contraction due to focal de-adhesion and actomyosin activity. The front-rear symmetry is primarily broken by the chemical polarization of the active and inactive Rho GTPase proteins, which govern the dynamics of the FA sites.

Here we generalize our previous multiscale framework for the talin-low cell migration, which accounted for this complexity by considering the feedback between the biological components in Fig 1 A, by including the effect of focal adhesion reinforcement due to talin unfolding (Fig 1 B) [28]. Our modified multiscale model takes into account the nonlinear strain-stiffening of the cytoskeleton and the augmented Stokes drag force on the deformed cell nucleus under cell flattening, as well as uses the standard linear solid (SLS) model for the ECM viscoelasticity. At the subcellular scale, a motor-clutch model with adhesion reinforcement is employed to determine the effect of substrate rigidity on traction forces at each FA site (Fig 1 C). Since cells operate in low Reynolds numbers, we only consider the viscous forces arising from the nucleus-cytoplasm and cell membrane-substrate frictions at the cellular scale. In our model, the forces across the two scales are

transmitted by the cytoskeleton, and the augmented Stokes drag force on the deformed cell nucleus in turn determines the active motion of the cell (Fig 1D and E).

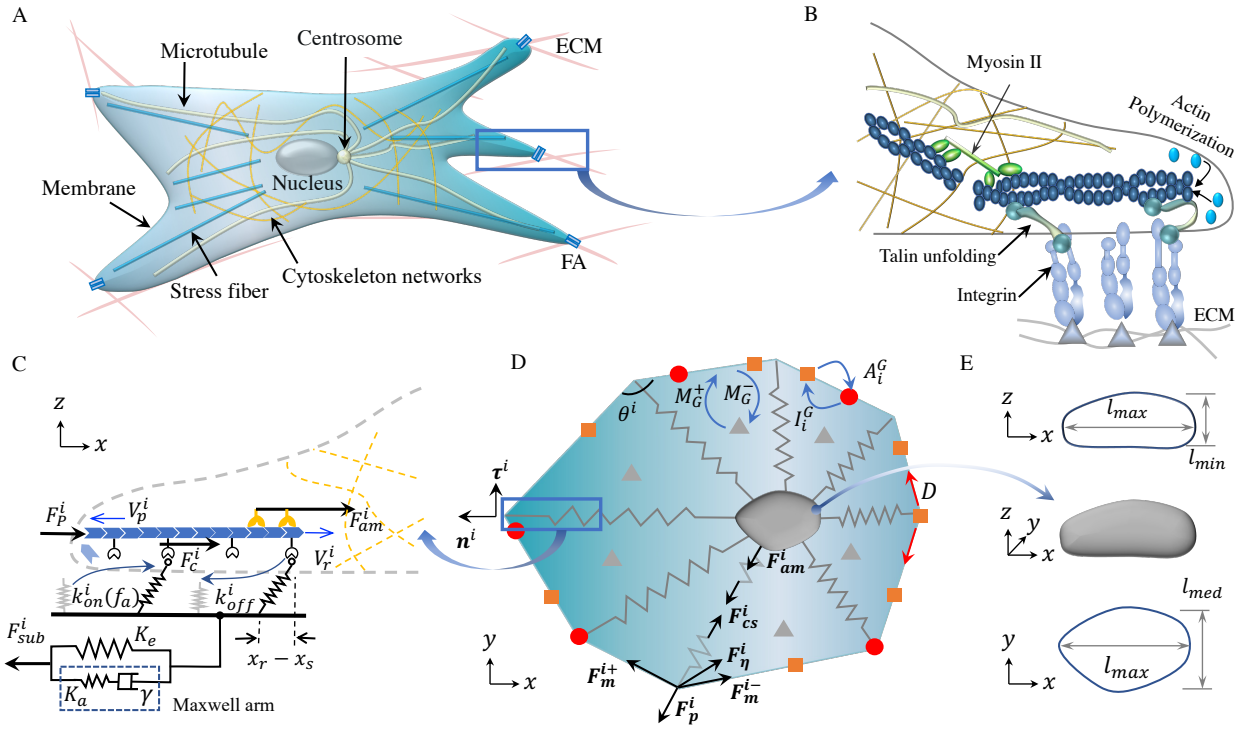

Figure 1: **Multiscale whole-cell theory schematics.** (A) Intracellular organization involved in mesenchymal migration. (B) Close-up view of the cytoskeleton–ECM linkage via integrins and the adaptor proteins (e.g., talin). (C) The parameters and variables of the motor-clutch model with adhesion reinforcement at each FA site. (D) The vertex-based model that couples the cell-matrix interactions at the subcellular scale to the chemomechanical dynamics at the cellular scale. The Rac1 concentration R and RhoA concentration ρ can each be in a membrane-bound active (red dots) or inactive state (orange squares), or dissolved in the cytoplasm (gray triangles). The conversion rates between these states are A_G^i , I_G^i , M_G^- , M_G^+ ($G \equiv \{R, \rho\}$), D is the diffusion constant of the membrane-bound species (Eq 16). The angle between the two membrane sections at a vertex is denoted by θ^i . (E) The principal dimensions l_{max} , l_{med} , l_{min} of a deformed nucleus.

Equations of motion at subcellular scale

We first present the calculation of the cell vertex displacements due to the FA site dynamics and the mechanical balance at the corresponding vertex. For a vertex i with position vector $\mathbf{x}^i(t)$, the local spreading velocity $\mathbf{V}_s^i \equiv \dot{\mathbf{x}}^i$ needs to be determined at every time step. In our model, the radial component $V_{s,n}^i \equiv \mathbf{V}_s^i \cdot \mathbf{n}^i$ is controlled by the active processes, i.e., actin polymerization and actomyosin contraction regulated by the Rho GTPase proteins, while the polar spreading speed $V_{s,\tau}^i \equiv \mathbf{V}_s^i \cdot \boldsymbol{\tau}^i$ is set by the balance between the polar components of the passive forces due to the cell deformations ($\mathbf{n}^i$, $\boldsymbol{\tau}^i$ defined in Fig 1 D).

The active radial spreading of a vertex with a speed $V_{s,n}^i$ is fueled mainly by F-actin formation with a polymerization speed V_p^i and counteracted by the retrograde G-actin flow with a speed V_r^i , which yields

$$V_{s,n}^i = V_p^i - V_r^i \,. \tag{1}$$

The polymerization rate at the vertex i is given by the ratio of the active Rac1 concentration R_a^i to its mean $\langle R_a^i \rangle$ averaged over all vertices as $V_p^i \equiv \frac{R_a^i}{\langle R_a^i \rangle} V_p^0$, where V_p^0 is the reference polymerization speed. The retrograde actin flow speed V_r^i is promoted by the net resistance force against protrusion F_p^i due to the cell membrane elasticity and myosin contractions (Fig 1B, C) and impeded by an elastic restoring force F_c^i due to the formation of molecular bonds by proteins such as integrins, talin, and vinculin between F-actin and ECM. We thus propose a phenomenological relation

$$V_r^i = V_0 \left\{ 1 - \frac{F_{am}^i}{N_m^i f_m} \right\} , \quad F_{am}^i \equiv F_c^i - F_p^i \,, \tag{2}$$

where $\{x\} \equiv \max(x, 0)$ is introduced to avoid a nonphysical retrograde flow velocity caused by numerical oscillations on a very stiff substrate (in general, $\{x\} = x$ in our simulations). V_0 is the unloaded myosin motor speed, N_m^i is the number of active myosin motors, and f_m is the force that stalls the activity of one myosin motor. RhoA is known to induce myosin motor activation, leading to stress fiber formation and contractility [43, 44]. Therefore, we assume that the myosin motor number is controlled by the active RhoA concentration ρ_a^i and its mean $\langle \rho_a^i \rangle$ averaged over all vertices as $N_m^i(t) \equiv \frac{\rho_a^i}{\langle \rho_a^i \rangle} N_m^0$, where N_m^0 is the reference myosin motor number. In Eq 2, the elastic restoring force F_c^i is determined from the FA dynamics with adhesion reinforcement, which is triggered by the stiffness of the viscoelastic substrate. On the other hand, the protrusion force F_p^i is set by the local force balance at each vertex in the presence of the nonlinear strain stiffening of the cytoskeleton. To calculate these two force strengths, we detail each of those processes next.

Focal adhesion dynamics with adhesion reinforcement. To account for the adhesion reinforcement due to talin unfolding, we extend the augmented motor-clutch model for FA dynamics introduced in Refs. [21, 23] in order to calculate clutch the force F_c^i at each vertex. By denoting average displacements of all bounded clutches at the filament end by $x_r^i(t)$ and the displacement of the substrate by x_{sub}^i , the engaged clutch is represented by a Hookean spring with tension $f_c^i = K_c(x_r^i - x_{sub}^i)$ (K_c : spring stiffness) [45, 46]. At

any instant t, the unbounded clutches must associate with a rate k_{on}^i. For the talin-low cells, a constant association rate k_{on}^0 is typically assumed, corresponding to a constant clutch binding timescale $\tau_{on}^0 \equiv 1/k_{on}^0$ [17, 23, 28]. We introduce the adhesion reinforcement by assuming that, when the time-averaged clutch force $\left\langle f_a^i \right\rangle_{\tau_l} \equiv \int_0^{\tau_l} f_c^i dt/\tau_l$ (τ_l : variable focal adhesion lifetime) is above a threshold force f_{cr} , the clutch binding rate will increase per [21, 23],

$$k_{on}^i = k_{on}^0 \left(1 + e^{\zeta(\left\langle f_a^i \right\rangle_{\tau_l} - f_{cr})}\right) , \tag{3}$$

where ζ is a characteristic inverse force scale. Note that $\left\langle f_a^i \right\rangle_{\tau_l}$ is time-dependent, and we update it every $N = 4000$ time steps (equivalent to a minute in real units) can accurately quantify the adhesion reinforcement regime while maintaining a reasonable computational cost. The procedure for the computation of $\left\langle f_a^i \right\rangle_{\tau_l}$ is explained in Supplementary methods and Fig A, B in S1 Text.

Once formed, the molecular clutches must unbind at a dissociation rate k_{off}^i that depends on the clutch tension f_c^i . To that end, we use the functional form $k_{off}^i \equiv k_{r0} \exp\left(f_c^i/f_{r0}\right) + k_{c0} \exp\left(-f_c^i/f_{c0}\right)$. Here, k_{r0} and k_{c0} denote the unloaded off-rate and the unloaded catch-rate, respectively, f_{r0} is the characteristic rupture force, and f_{c0} is the characteristic catch force. It follows that the fraction of the engaged clutches $(0 \leq P^i(t) \leq 1)$ is governed by the mean-field rate equation [45, 23, 46],

$$\frac{dP^i}{dt} = k_{on}^i \left(1 - P^i\right) - k_{off}^i P^i \, . \tag{4}$$

Denoting the number of available clutches as N_c^i, the total clutch force at the vertex i is then given by $F_c^i = P^i N_c^i f_c^i$. Here we incorporate the critical role of the Rac1 proteins in focal complex assembly by relating N_c^i to the local Rac1 concentration, i.e., $N_c^i(t) \equiv \frac{R_a^i}{\langle R_a^i \rangle} N_c^0$, where N_c^0 denotes the reference clutch number [47, 48, 49]. The mechanical equilibrium condition at the cell-substrate interface demands that the total force sustained by the engaged clutches must be balanced by the substrate deformation, leading to

$$F_{sub}^i = F_c^i = P^i N_c^i K_c \left(x_r^i - x_{sub}^i\right) \, . \tag{5}$$

In Eq 5, the substrate displacement x_{sub}^i is an unknown to be determined from a constitutive model for the substrate viscoelasticity, which we focus on next.

Constitutive model for substrate viscoelasticity. Our previous implementation utilized the classical Kelvin-Voigt model for the substrate relaxation dynamics [28]. However, since the Kelvin-Voigt model predicts a very rigid nonphysical behavior when $t < \tau_r$ (τ_r : substrate relaxation timescale) [50], it can result in a premature adhesion reinforcement. Comparatively, the standard linear solid (SLS) model allows for a better physical modeling by including a Maxwell arm (Fig 1) [51]. It has also been demonstrated that the SLS model can capture the prominent relaxation timescale of the viscoelastic substrates fabricated by combining covalent and supramolecular crosslinking [23]. The SLS model expresses the constitutive relationship between x^i_{sub} and the substrate force F^i_{sub} as (Fig 1 C)

$$(K_e + K_a)\gamma \dot{x}^i_{sub} + K_a K_e x^i_{sub} = K_a F^i_{sub} + \gamma \dot{F}^i_{sub}\,, \tag{6}$$

where K_e is the elastic stiffness at $t \to \infty$, γ is the substrate viscosity, and K_a is the additional stiffness that governs the substrate relaxation with a timescale $\tau_r \equiv \gamma/K_a$. A stress relaxation test from a constant strain yields the instantaneous and long-term stiffness of the substrate as $K_{t\to 0} = K_e + K_a$ and $K_{t\to\infty} = K_e$, respectively. The instantaneous stiffness $K_{t\to 0}$ characterizes the initial elastic response of the substrate when the viscous deformation and stress relaxation have not yet taken place in the limit $t \to 0$. Thus, cells with a very short focal adhesion lifetime ($\tau_l < \tau_r$) can only sense the instantaneous stiffness. In contrast, the long-term stiffness $K_{t\to\infty}$ refers to the residual substrate stiffness after the viscous stresses have relaxed.

Cytoskeletal stiffening. The passively deforming cell cytoskeleton, which consists of microtubules and intermediate filaments, is represented by multiple springs in our model (Fig 1 D). Here we will assume that these cytoskeletal "springs" undergo strain-stiffening during large spreading events and thus exhibit nonlinear elasticity. This assumption is backed by the experiments performed, e.g., on NIH-3T3 fibroblasts that reveal a strong correlation between the cell rigidity and cell area during large spreading events [8]. Assuming this behavior is mechanically driven and thus must be generic across animal cells, we propose a phenomenological equation for the cytoskeletal stiffness K_{cs} in terms of the cell area A: Denoting the position vector of the cell nucleus by $\mathbf{x}_{nuc}$ and defining the length of a cytoskeletal spring as $r^i \equiv |(\mathbf{x}_{nuc} - \mathbf{x}^i)|$, the cytoskeletal restoring force in our model is governed by the differential equation

$$\frac{dF^i_{cs}}{dr^i} = K_{cs}(A) = K^b_{cs} + \Delta K_{cs} e^{\beta A}\,, \tag{7}$$

where K_{cs}^b denotes the baseline stiffness. The term $\Delta K_{cs} e^{\beta A}$ is introduced to describe the exponential hyperelastic behavior [52, 53], with the values of ΔK_{cs} and β obtained through linear regression of the experimental data in [8] (See Sec 1.2 and Fig C (A) in S1 Text).

Local mechanical equilibrium. We enforce local force balance at each vertex to determine the radial protrusion force F_p^i and the polar spreading speed $V_{s,\tau}^i$. The cell membrane is modeled as a closed loop of Hookean springs with stiffness K_m between adjacent vertices, resulting in tensile forces at the ith vertex of $\mathbf{F}_{m,\pm}^i = K_m(\mathbf{l}_\pm^i - \mathbf{l}_0)$, where $\mathbf{l}_+^i$ and $\mathbf{l}_-^i$ are the distance vectors between vertex i and its two neighbors, and $\mathbf{l}_0$ is the initial distance between two adjacent vertices. Due to the interactions between the cell membrane and extracellular medium, the viscous force strength on vertex i is expressed as $F_\eta^i = \eta_m^i l^i \mathbf{V}_s^i$, where $l^i \equiv (|\mathbf{l}_+^i| + |\mathbf{l}_-^i|)/2$ defines the average membrane length about the ith vertex. In addition to the membrane forces, each vertex experiences a protrusion force F_p^i and a cytoskeletal radial force F_{cs}^i . Thus, the net force balance at each vertex in the radial direction $\hat{\mathbf{n}}^{\mathbf{i}}$ and the polar direction $\hat{\boldsymbol{\tau}}^i$ is given by

$$F_p^i - F_{cs}^i + \left(\mathbf{F}_{m,+}^i + \mathbf{F}_{m,-}^i\right) \cdot \hat{\mathbf{n}}^{\mathbf{i}} - \eta_m l^i V_{s,n}^i = 0\,, \tag{8a}$$

$$\left(\mathbf{F}_{m,+}^i + \mathbf{F}_{m,-}^i\right) \cdot \boldsymbol{\tau}^i - \eta_m l^i V_{s,\tau}^i = 0\,. \tag{8b}$$

Eq 8a and 8b yield F_p^i and $V_{s,\tau}^i$, respectively. Altogether, Eq 1–8b fully determine the vertex spreading velocities $\mathbf{V}_s^i$ when the nucleus displacement $\mathbf{x}_{nuc}$ and the dynamical GTPase concentrations at each vertex are computed at the cellular scale.

Equations of motion at cellular scale

Next, we explain the global mechanical equilibrium that governs the nucleus motion and the intracellular Rho-GTPase dynamics, which directly influence the aforementioned subcellular processes.

Modified Stokes' law for deformed nucleus motion. Our model quantifies the cell translocation by the net translation of the cell nucleus, which balances the forces between the cytoskeletal microtobule and intermediate filament bundles. At the cell periphery, these cytoskeletal complexes are linked to the F-actin

at the FA sites, transmitting the net traction force from the extracellular matrix (F^i_{sub}) and the protrusion force from the cell boundary (F^i_p) to the cell nucleus (Fig 1). This tight linkage to the rest of the cell can deform the nucleus when the cell flattens under large spreading on stiff substrates [29]. To balance these peripheral and cytoskeletal forces, the nucleus undergoes viscous drag within the cytoplasm while it deforms under cell flattening. We use a modified Stokes' law for the effect of nucleus deformation to the drag force,

$$\mathbf{F}^{\eta}_{nuc} = -6\pi f_{shape}\eta_{cp} r^0_{nuc}\dot{\mathbf{x}}_{nuc}\,, \tag{9}$$

where r^0_{nuc} represents the radius of a spherical nucleus, f_{shape} is the shape factor characterizing the deviation from a sphere such that $f_{shape} = 1$ for a sphere, and η_{cp} is the cytoplasm viscosity.

The shape factor can be conveniently given by the Corey shape function (CSF) in terms of the three principal lengths of the nucleus as (Fig 1 E) [54, 55]

$$f_{shape} = \left(\frac{l_{max}l_{med}}{l^2_{min}}\right)^{\alpha}\,, \tag{10}$$

where the exponent $\alpha = 0.09$ was obtained by fitting the experimental drag coefficient of non-spherical particles under Stokes flow [55]. For the deformed nucleus, the longest and the shortest dimensions define the aspect ratio (Fig 1 E), which can be related to the cell spreading area by

$$\delta \equiv \frac{l_{max}}{l_{min}} = \chi A + 1\,. \tag{11}$$

We obtained the exponent $\chi = 0.0024$ by fitting the experimental cell shape data in Ref. [56] (Fig C (B) in S1 Text). The intermediate dimension l_{med} corresponds to the length of the minor axis of the nucleus on the $x - y$ plane, and it was found to have a constant ratio to the length of the major axis in experiments ($l_{med} = 0.8 l_{max}$) [29]. Consequently, the nucleus shape factor can be expressed as a function of the cell spreading area A by substituting Eq 11 into Eq 10,

$$f_{shape} = 0.98\,(\chi A + 1)^{2\alpha}\,. \tag{12}$$

Experiments have demonstrated that the cytoplasm viscosity, like the strain stiffening, is strongly correlated with the cell spreading area [31, 32]. These experiments also indicate that the cell viscosity and cell

stiffness exhibit the same trend with increasing substrate stiffness. Therefore, we assume an area-dependent cytoplasm viscosity (similar to that in Eq 7) as

$$\eta_{cp}(A) = \eta_{cp}^0 + \Delta\eta_{cp} e^{\beta A} \,, \tag{13}$$

where η_{cp}^0 is the cytoplasm viscosity on soft substrates [57] and $\Delta\eta_{cp}$ controls the rate of viscosity increase with the cell spreading area A .

At the frame of the nucleus, the condition for the mechanical equilibrium between Eq 9, the cytoskeletal and the subcellular forces

$$\sum_{i=1}^{N} \left(F_{sub}^i + F_{cs}^i - F_p^i \right) \hat{\mathbf{n}}^i - \mathbf{F}_{nuc}^{\eta} = 0 \tag{14}$$

yields the nucleus migration velocity, $\dot{\mathbf{x}}_{nuc}$, equivalent to the cell velocity in our model.

Reaction-diffusion dynamics of GTPase concentrations. As with our previous work [28], here we adopt the biochemical reaction-diffusion equations introduced in [58, 59] to describe the dynamics of active and inactive GTPases. The model tracks the volume fractions of the signaling proteins in three forms: the active membrane-bound form $(G_a^i(t) \equiv \{R_a^i(t)\,, \rho_a^i(t)\})$, the inactive membrane-bound form $(G_{in}^i(t) \equiv \{R_{in}^i(t)\,, \rho_{in}^i(t)\})$, and the inactive cytosolic form $(G_{cp}(t) \equiv \{R_{cp}(t)\,, \rho_{cp}(t)\})$. We assume $G_{cp}(t)$ to be evenly distributed in the cytosol at all times, while the membrane-bound forms diffuse across the vertices. The corresponding diffusive fluxes are given by the Fick's law in a finite difference formulation as

$$J_y^i \equiv -D \left(\frac{G_y^{i+1}/\langle l^{i+1} \rangle - G_y^i/\langle l^i \rangle}{|\mathbf{l}_+^i|} \right) \,. \tag{15}$$

Eq 15 takes into account the effect of the deformed cell shape on the diffusive flux by updating the vertex coordinates at each time step. Different forms of the proteins on a vertex are interconvertible with the inactive-to-active rates A_G^i , active-to-inactive rates I_G^i, and inactive-to-cytosolic association and disassoci-

ation rates M_G^+ , M_G^- (Fig 1 D). Altogether, the reaction-diffusion kinetics is governed by

$$\begin{cases} \dot{G}_a^i = A_G^i G_{in}^i - I_G^i G_a^i + \left(J_a^{i-1} - J_a^i\right) , \\ \dot{G}_{in}^i = -A_G^i G_{in}^i + I_G^i G_a^i + \left(J_{in}^{i-1} - J_{in}^i\right) + \dfrac{M_G^+ G_{cp}}{N} - M_G^- G_{in}^i , \\ \dot{G}_{cp} = -M_G^+ G_{cp} + \sum_{i=1}^{N} M_G^- G_{in}^i . \end{cases} \tag{16}$$

The active Rac1 and RhoA GTPase volume fractions R_a^i , ρ_a^i regulate the cell migration by controlling the actin polymerization speed V_p^i (Eq 1), the number of myosin motors N_m^i (Eq 2), and the clutch number N_c^i at each FA site (Eq 5). Different from Refs. [58, 59], the rate terms A_G^i in our formulation account for the reverse coupling from the cell deformation to the signaling pathways in addition to the mutual inhibition of the Rac1 and RhoA (See S1-Appendix). Since the filopodial protrusions of a mesenchymal cell grow and shrink at timescales comparable to the migration times, this chemo-mechanical feedback prevents the Rac1 and RhoA dynamics from reaching a steady bistable polarized state. Instead, when the transient chemical polarity ceases, our simulation algorithm reinstates the polarization stochastically to sustain the random migration patterns in many mesenchymal phenotypes [26, 27].

Simulation procedure

We represent the initial vertex configuration of the cell as a regular 16-sided polygon due to its decent convergence properties [28]. All initial forces, velocities, displacements, and substrate deformations are set to zero. Since chemical signaling drives cell polarization followed by directional locomotion on uniform substrates [28], a nonuniform initial distribution of the active Rac1 protein volume fraction R_i^a is enforced with a higher value at the cell front. Likewise, a polarized initial distribution of the active RhoA protein volume fractions ρ_i^a is taken with accumulation at the cell rear (manual polar symmetry breaking). In contrast, the initial conditions for R_{in}^i, ρ_{in}^i are uniform at time $t = 0$, and the cytoplasmic form R_{cp}, ρ_{cp} can be determined from the total volume fraction conservation (Fig D in S1 Text). For directed migration on nonuniform substrates, uniform initial signaling distributions must be assumed since the polarity will be set by the gradients of the ECM stiffness or viscosity. Starting from these initial conditions, the vertex spreading and the nucleus velocities are calculated by solving Eq 1–14, and the Rho-GTPase volume fractions are updated by solving Eq 15, 16 by following the algorithm in Fig B in S1 Text. When the cytoplasmic inactive Rac1

Table 1: **Residual substrate stiffness K_e , additional stiffness K_a , and viscosity γ ranges in simulations.**

Parameter	Real units	Dimensionless units
K_e	0.1-100 pN/nm [17, 23, 46]	$5\pi - 5000\pi$
K_a	$0.1 - 20\, pN/nm$	$20\pi - 4000\pi$
γ	$0.01 - 100.0\, pN{\cdot}s/nm$ [23]	$0.06 - 60$

volume fraction R_{cp} reaches a steady state, we reinitialize R_a^i and ρ_a^i stochastically to mimic the random nature of the protrusion formations in the mesenchymal cells. To incorporate the adhesion reinforcement (Eq 3), we fix $\zeta = 0.5pN^{-1}$ since it leads to a good agreement between the simulated spreading areas and the experimental data in Ref. [8] (Fig E in S1 Text). The parameters $\Delta K_{cs} = 2.8\, pN/\mu m$ and $\beta = 0.00185$ (Eq 7) and $\chi = 2.4 \times 10^{-3}$ (Eq 12) provide the best fit to the experimental data from Ref. [8] and are kept constant in all simulations (See Sec 1.2 and Fig C in S1 Text). All fixed simulation parameters are listed in Table A in S1 Text.

We present the simulation results in dimensionless form by introducing a position scale $L \equiv 2\pi r_0 = 10\pi\ \mu m$, speed scale $V_0 = 120\ nm/s$, migration timescale $T \equiv L/V \approx 260\ s$, and force scale $F_0 \equiv N_m^0 f_m = 200\ pN$. For each simulation, we run $M > 10^6$ time steps with a time step of approximately $\Delta t \approx 10^{-3}\ s$ ($\Delta t \approx 10^{-5}$ in dimensionless units), corresponding to the migration dynamics over at least an hour in real units. The spreading area A is calculated as the average cell area over the last 10^6 time steps in a simulation. We define the migration speed V as the nucleus trajectory length $X \equiv |\mathbf{x}_{nuc}(M\Delta t) - \mathbf{x}_{nuc}(0)|$ divided by the total time $t_{total} \equiv M\Delta t$, i.e., $V \equiv L/t_{total}$. The ranges of the ECM material parameters used in the simulations are listed in Table 1. For each set of the ECM parameters, we run n simulations to compute the sample mean spreading area, $\overline{A}$, and the mean migration speed, $\overline{V}$. The effects of the ECM viscoelasticity on the spreading area, migration speed, and migration direction are validated by the experimental data taken from Refs. [6, 27, 16].

Results

Simulations reproduce experimental cell spreading and migration speed dependence on substrate stiffness

With increasing stiffness K_e on an elastic substrate ($\gamma = 0$, $K_a = 0$), the cell spreading area increases monotonically, in agreement with the experiments on the adhesion-reinforced U373-MG human glioma cell spreading on polyacrylamide hydrogels (Fig 2 A) [6]. This can be understood by inspecting the FA

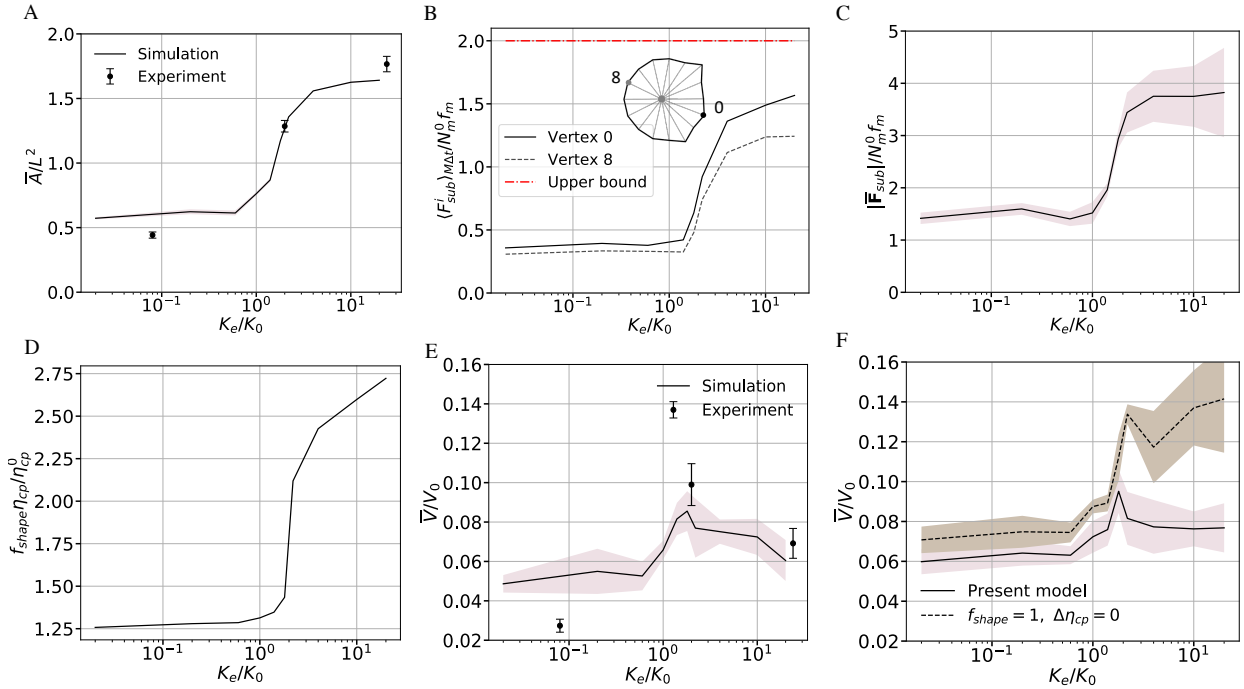

Figure 2: **Cell spreading area and migration speed on elastic substrates.** (A) The dimensionless mean cell area $\overline{A}/L^2$ (full line) as a function of the dimensionless substrate elastic stiffness K_e/K_0 . For comparison, the dots and error bars are the experimental data from Ref. [6, 60]. (B) The average dimensionless substrate traction force versus K_e/K_0 at vertex 0 (cell front) and vertex 8 (cell rear). The red dash-doted line gives the upper bound of the substrate traction force on very stiff substrates. The calculation of the averaged substrate traction forces $\left\langle F^i_{sub}\right\rangle_{t_{total}}$ from the full focal adhesion cycles is illustrated in Fig F in S1 Text. (C) The dimensionless mean and standard deviations of the net traction force versus K_e/K_0 . The calculation of the time-averaged net traction force is illustrated in Fig G in S1 Text. (D) Cell-spreading induced nucleus viscous drag increase $f_{shape}\eta_{cp}/\eta^0_{cp}$ versus K_e/K_0 , which is calculated by using Eq 9, 12, 13 for the mean spreading area values in A. (E) The simulated dimensionless mean migration speed $\overline{V}/V_0$ versus K_e/K_0 (full curve) and the experimental data for the U373-MG human glioma cells (dots and error bars) [6]. (F) The influence of the shape factor f_{shape} of the deformed nucleus and the area dependent cytoplasm viscosity η_{cp} on the migration speed (Eq 12, 13). The mean values or the standard deviations are calculated over $n = 10$ simulations at each data point in A, C, D, E, F.

dynamics at the subcellular scale: According to Eq 2, 5, the cell spreading speed at a vertex $V^i_{s,n}$ is set by the competition between the polymerization speed V^i_p and the actin retrograde flow speed V^i_r , which is counteracted by the stiffness-dependent focal traction force (See S2-Appendix)

$$F_{sub} = N^0_m f_m \left(1 - e^{-t/\tau_l}\right) , \quad \tau_l \equiv \frac{N^0_m f_m}{V_0 K_e} . \tag{17}$$

Eq 17 is derived for an isolated motor clutch system where the engaged clutch fraction is assumed to be saturated on a compliant substrate ($P^i \approx 1\,;\, K_e \ll N^0_c K_c$) . For sufficiently low K_e where the adhesion

Table 2: **Characteristic scales for spreading and migration dynamics.** For a viscoelastic substrate, K_a is the additional stiffness, and γ is the viscosity in the SLS model. Additionally, N_m^0 is the reference myosin motor number, V_0 is the unloaded myosin motor speed, f_m is the force that stalls the activity of one myosin motor, and k_{on}^0 denotes the reference clutch binding rate. The scales denoted by * are valid for substrates with a stiffness lower than K_0 .

Quantity	clutch binding timescale*	clutch lifetime*	threshold stiffness	substrate relaxation timescale	optimal viscosity
Definition	$\tau_{on}^0 \equiv \frac{1}{k_{on}^0}$	$\tau_l \equiv \frac{N_m^0 f_m}{V_0 K_e}$	$K_0 \equiv \frac{N_m^0 f_m k_{on}^0}{V_0}$	$\tau_r \equiv \frac{\gamma}{K_a}$	$\gamma_0 \equiv \frac{K_a}{k_{on}^0}$
Value	$1/3\ s$	$1/3 - 50/3\ s$	$\approx 5.0\ pN/nm$	$10^{-2} - 10^2\ s$	$\leq 5/3\ pN \cdot s/nm$

reinforcement mechanism is not triggered (see Eq 3), the traction force starts building up at an FA site after the molecular clutches form at a timescale $\tau_{on}^0 \equiv 1/k_{on}^0$, and develops with a characteristic time τ_l (Eq 17). The comparison between the two timescales ($\tau_{on}^0 = \tau_l$) defines a threshold stiffness $K_0 \equiv N_m^0 f_m k_{on}^0 / V_0 \approx 5\ pN/nm$ (Table 2). On soft substrates ($K_e \leq K_0$), since the force build-up time τ_l is much longer than the clutch formation time τ_{on} , the adhesion force mostly remains low, i..e, $F_{sub}^i < N_m^0 f_m$ (Eq 17; Fig 2 B). For a stiff substrate with $K_e > K_0$, the decrease in the force build-up time τ_l must cause a steep increase in the average force per bond ($\langle f_a \rangle_{\tau_l} > f_{cr}$), triggering the adhesion reinforcement mechanism with an augmented binding rate k_{on} (Eq 3, Fig A in S1 Text). The reinforced binding rate can even saturate the bounded clutches on a very stiff substrate, i.e., $P^i \to 1$ (See Fig A(F) in S1 Text). Moreover, a higher $\langle f_a \rangle_{\tau_l}$ on stiff substrates lead to higher disassociation rates k_{off} , which must balance the binding rate in Eq 4 to reach a steady bound clutch fraction $P^i \sim 1$. This condition yields an estimate for the instantaneous force per bond as $f_c^i \propto \zeta(\langle f_a \rangle_{\tau_l} - f_{cr}) f_{r0}$ (See S3-Appendix). This allows us to estimate an upper bound of the substrate traction force on a stiff substrate as $F_{sub}^i = N_c^i f_c^i \approx 8\zeta N_c^i > N_m^0 f_m$, in agreement with the simulations (Fig 2 B). This elevated traction at $K_e > K_0$ across the cell is the main driving factor behind enhanced cell spreading. Furthermore, the Rho GTPase polarization leads to a higher traction force at the cell front than at the rear since the motor clutch number N_c^i is controlled by the Rac1 concentration (Fig 2 B). Due to the chemically induced polarization, the cell acquires a larger net traction force on stiff substrates than on soft ones (Fig 2 C).

The cell motility is governed by the competition between the net traction force and the viscous drag of the nucleus since the remaining forces are negligible in Eq 14 (Fig H in S1 Text). Because large cell spreading on stiff substrates can deform the nucleus (Fig 2 D) and alter the cytoplasmic viscosity (Eq 13), the Stokes' drag force on the nucleus must increase, resisting the net traction force. Consequently, the

migration efficiency decreases beyond the threshold stiffness K_0, creating a biphasic stiffness-speed profile, which also quantitatively reproduces the U373-MG human glioma cell speed on polyacrylamide hydrogels (Fig 2 E) [6]. In our simulations, ignoring the nucleus shape change and assuming constant cytoplasmic viscosity recovers a monotonic relationship between the migration speed and substrate stiffness, which validates their role in the biphasic speed-stiffness relation (Fig 2 F).

Substrate viscosity affects cell spreading area and migration speed

We next discuss the effect of substrate viscosity on the cell area and migration speed on a substrate that is soft in the long time limit, $K_e = 0.1\ pN/nm$. When $K_e + K_a < K_0$ (soft regime), the adhesion reinforcement effect can be neglected even on viscous substrates. However, when $K_e + K_a \geq K_0$ (stiff regime), a large viscosity may trigger the adhesion reinforcement regime and alter the spreading behavior. We discuss both regimes below.

On substrates with a low instantaneous stiffness ($K_e + K_a < K_0$), the cell spreading area varies in a biphasic manner with increasing viscosity (Fig 3 A, B). This can be explained by examining the FA dynamics at the subcellular scale, similar to the cell spreading on elastic substrates. At an FA site without adhesion reinforcement, time averaging the traction force (see Fig I (A, B) in S1 Text) over a clutch lifetime τ_l leads to (See S2-Appendix)

$$\left\langle F^i_{sub} \right\rangle_{\tau_l} \approx \begin{cases} N^0_m f_m \exp\left[\dfrac{-\tau_l}{\tau_l + \tau_r(1 + \frac{K_a}{K_e})}\right] \text{ , if } \tau_r \leq \tau^0_{on} & \text{(18a)} \\ N^0_m f_m \exp\left(-1\right) \text{ , if } \tau_r \geq \tau_l \text{ ,} & \text{(18b)} \end{cases}$$

where the timescales τ_l , τ^0_{on} , τ_r are defined in Table 2. Eq 18a indicates that the average traction force at an FA site must increase with increasing viscosity when $\tau_r \leq \tau^0_{on}$. At $\tau_r > \tau^0_{on}$, since slower substrate relaxation leads to the FA lifetime reduction when (Fig I (C) in S1 Text), the average traction force should exhibit a decreasing profile with a lower bound that is estimated in Eq 18b. That way, Eq 18 indicates the presence of a non-monotonic traction force-viscosity profile in an isolated motor-clutch system on soft substrates. Note that when $\tau^0_{on} < \tau_r < \tau_l$, the average substrate force is not amenable to an analytical approximation. Still, given the biphasic profile suggested by Eq 18, it is plausible to assume that the average substrate force reaches a maximum when $\tau_r \approx \tau^0_{on}$, equivalently at an optimal viscosity $\gamma_0 \equiv K_a \tau^0_{on}$

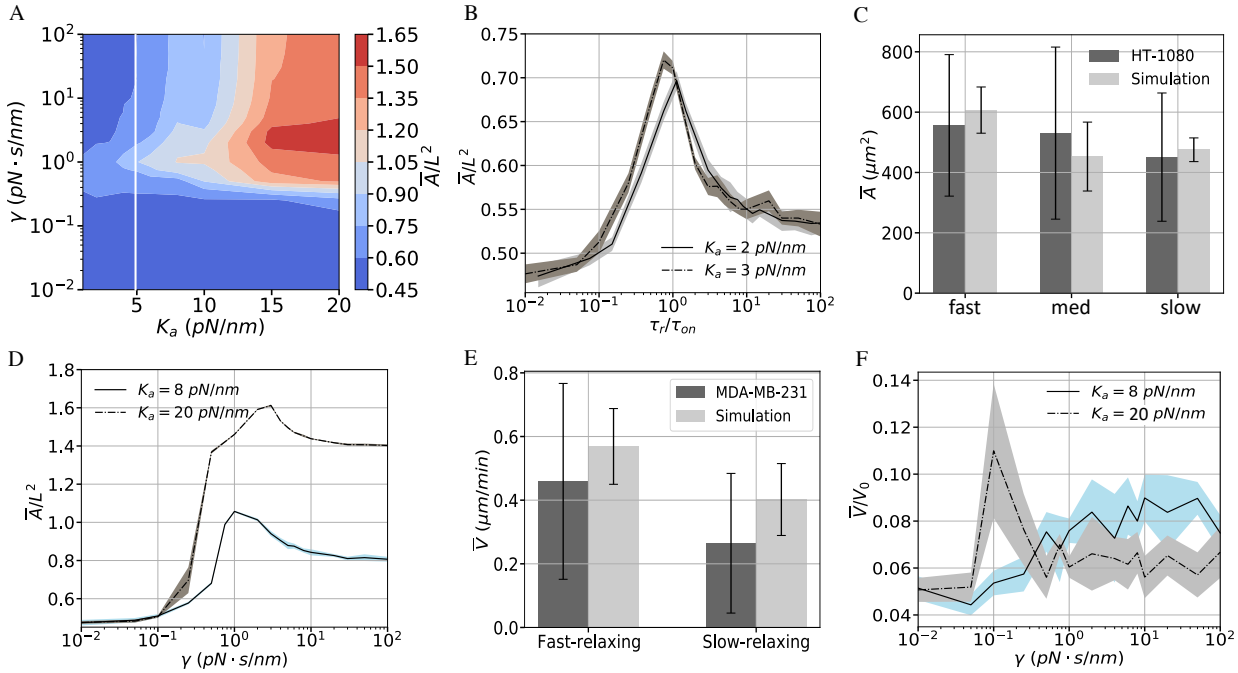

Figure 3: **Effect of substrate viscosity on spreading area and migration speed.** (A) Contour plot of the mean dimensionless cell area $\overline{A}/L^2$ on viscoelastic substrates as a function of the additional stiffness K_a and substrate viscosity γ ($K_e = 0.1\ pN/nm$). The white line denotes the threshold stiffness K_0 . (B) $\overline{A}/L^2$ and its standard deviation (shaded area) versus the ratio of the material relaxation timescale $\tau_r \equiv \gamma/K_a$ to the clutch binding timescale $\tau_{on}^0 \equiv 1/k_{on}^0$ on soft substrates. (C) For a fixed instantaneous stiffness $K_e + K_a = 2.6\ pN/nm$, the simulated spreading area $\overline{A}$ and its standard deviation ($n = 50$; light bars) and experimental data for HT-1080 cells (dark bars; data from [27]). By fitting the stress-time data in the stress relaxation test, the viscosities of the fast, intermediate (med), and slow relaxing substrates are found as $\gamma_{fast} = 1\ pN \cdot s/nm$, $\gamma_{med} = 60\ pN \cdot s/nm$, $\gamma_{slow} = 360\ pN \cdot s/nm$ (Fig J in S1 Text). (D) The dimensionless spreading area $\overline{A}/L^2$ and its standard deviation as a function of γ for different $K_a > K_0$. Since the clutch binding timescale τ_{on} depends on the adhesion reinforcement on stiff substrates, $\overline{A}/L^2$ is plotted against the substrate viscosity γ . (E) The mean migration speed $\overline{V}$ and its standard deviation in the simulations ($n = 50$; light bars) versus experiments of HT-1080 cells (dark bars; data from [27]) on fast-relaxing and slow-relaxing soft substrates, for which the material parameters are extracted from fitting the stress-time data (Fig J in S1 Text). (F) The dimensionless mean migration speed $\overline{V}/V_0$ and its standard deviation as a function of γ for two additional stiffness values $K_a = 8\ pN/nm$ and $K_a = 20\ pN/nm$. The contour plot in A contains 180 data points. The mean and standard deviations are calculated with $n \geq 5$ simulations at each point in B, D, F.

(Fig I (C) in S1 Text), thereby maximizing the cell spreading area. To further validate our model, we simulated spreading areas of human fibrosarcoma cells HT-1080 on viscoelastic substrates consisting of interpenetrating alginate networks (IPN) [27]. The experimental material parameters of the substrates with different relaxation rates were obtained by data fitting to the stress relaxation tests in Ref. [27] (See Sec 1.2 and Fig J in S1 Text). Our whole-cell model accurately replicates the experimentally observed spreading areas of the HT-1080 cells on soft substrates with different stress relaxation rates (Fig 3 C), indicating that

cell spreading is suppressed with increasing viscosity when $\tau_r > \tau_{on}^0$.

At a larger instantaneous substrate stiffness $K_e + K_a \geq K_0$, the cells only perceive the long-term stiffness K_e and maintain small spreading areas at a low substrate viscosity γ (Fig 3 D). For higher γ , the slowly relaxing substrate maintains the stiffness $K_e + K_a \geq K_0$ at later times, sustaining the adhesion reinforcement regime and thus promoting cell spreading. Moreover, because the adhesion reinforcement effect becomes more pronounced on stiffer substrates, a larger additional stiffness, such as $K_a = 20\, pN/nm$ further increases the cell spreading area at high γ (Fig 3 D).

As opposed to the spreading area that can be understood at the single FA level, the change in the cell migration speed as a function of γ must be examined by virtue of the net traction force $\sum_i \mathbf{F}_{sub}^i$ at the cellular scale. At an instantaneous substrate stiffness $K_a + K_e < K_0$, where the adhesion reinforcement is not activated, the high viscosity of $\gamma > \gamma_0$ can result in a decrease of the FA lifetime and thus a lower traction force (See S2-Appendix and Fig I (D)). Our simulations reveal that migration on fast relaxing substrates ($\tau_r \sim \tau_{on}^0$) is more efficient than on slow relaxing substrates ($\tau_r \gg \tau_{on}^0$) (Fig 3 E). This is in quantitative agreement with the migration speeds of the MDA-MB-231 human breast cancer adenocarcinoma cells on fast and slow relaxing IPN [27]. A more comprehensive parametric study demonstrates the presence of a biphasic speed-viscosity relation (Fig K (A, B) in S1 Text). The optimal viscosity corresponding to the maximum migration speed tends to be slightly higher than γ_0 (for maximum cell spreading), primarily due to the prolonged FA lifetime at the front of the cell (See S2-Appendix). On substrates with high instantaneous stiffness ($K_a + K_e \geq K_0$), the net traction force increases with viscosity due to the adhesion reinforcement effect (Fig K (C)). Since cells have limited spreading areas due to the weak engagement of the adhesion reinforcement regime at $K_a = 8\, pN/nm$ (Fig 3 D), the change in the nucleus drag force is marginal. Thus, we obtain a nearly monotonic increase in the migration speed with viscosity (Fig 3 F). However, with a very large additional stiffness of $K_a \gg K_0$, strong adhesion reinforcement on the viscous substrate results in very large spreading areas (Fig 3 D), which significantly increases the nucleus drag forces and in turn leads to a biphasic speed-viscosity profile (Fig 3 F).

Migration direction is set by stiffness or viscosity variation on nonuniform substrates

Having elucidated the effect of substrate stiffness and viscosity on cell area and migration speed, we investigate the sensitivity of cell migration to a stiffness gradient on elastic substrates or a viscosity gradient on viscoelastic substrates. To eliminate the effect of chemical polarity on migration direction in the simulations,

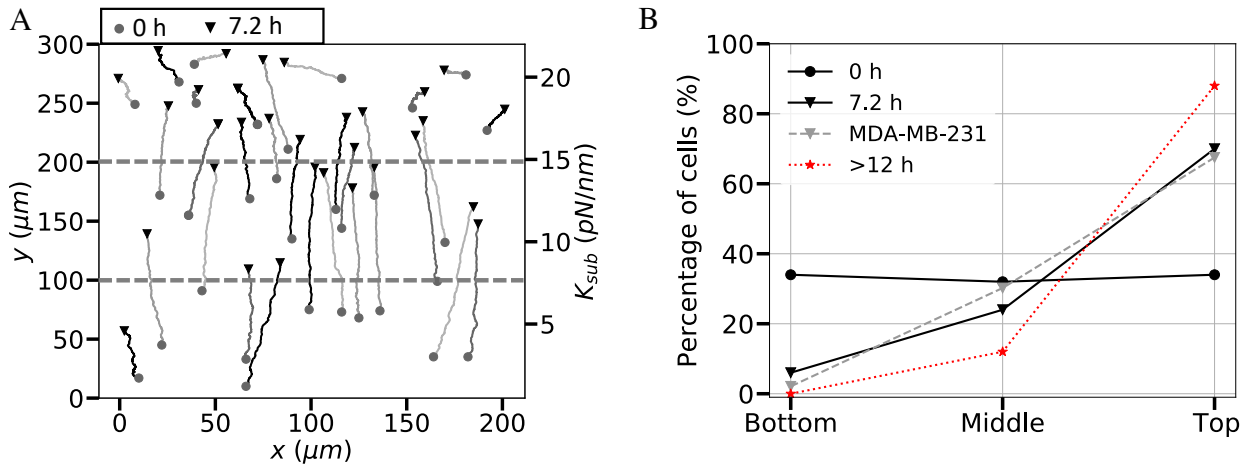

Figure 4: **Simulations reproduce cell durotaxis on elastic gradient substrates.** (A) Trajectories of 30 simulated cells over > 7.2 hours in real units on an elastic substrate with a linear stiffness variation between $K_e = 0.5 - 22\ pN/nm$ in the $y-$direction. (B) The percentage of the simulated cells out of $n = 83$ simulations on the bottom-, middle-, and top-third of the gradient substrate as a function of time, i.e., at $t = 0\ h$ (initial condition), $t = 7.2\ h$, $t > 12\ h$, which are compared to the distributions of the MDA-MB-231 cells (gray dashed lines) that are seeded on polyacrylamide hydrogels with a stiffness gradient and observed for 72 hours [16].

we specify the initial conditions of a chemical apolar cell by assigning a random distribution of the active Rac1 concentration R_a^i and setting the other membrane-bound Rho GTPase concentrations ρ_a^i , R_{in}^i , ρ_{in}^i constant (Fig L in S1 Text). We compared our migration simulations of 83 cells on elastic gradient substrates to the experimental migration patterns of the MDA-MB-231 cells on polyacrylamide hydrogels with a stiffness gradient $0.5-22.0\ kPa$ [16]. For computational efficiency, we consider a $200\mu m \times 300\mu m$ domain at about a $1:10$ scale of the experimental platform (Fig 4 A). We record the migration trajectory of each simulated cell for 7.2 hours, which is $1/10$ of the experimental observation time ($72\ h$). Due to the difficulty in quantifying the substrate gradient in the experiments, we assume a constant gradient $\nabla K_e \approx 72\ pN/\mu m^2$ in the $+y-$direction in the simulations; non-dimensionalization by the initial cell diameter $2r_0$ and the threshold stiffness K_0 yields the unitless gradient $\tilde{\nabla}\tilde{K_e} \approx 0.14 < 1$. The simulated cell trajectories indicate that all cells with random locations at $t = 0$ move up the stiffness gradient regardless of their initial positions, i.e., the cells undergo robust durotaxis (Fig 4 A). Also, the percentages of the simulated cells in three substrate portions demonstrate the strong migration trend towards the stiffest region (Fig 4 B), in good agreement with the gradient sensitivity of the MDA-MB-231 cells with talin- and vinculin-mediated FA formations [16]. We further confirm that almost all cells eventually migrate to the stiffest region after $> 12\ h$ (Fig 4 B). The robust durotaxis behavior is mainly due to the monotonic increase of the traction force as a function of

the substrate stiffness at an FA site due to the adhesion reinforcement (Fig 2 B). In other words, the FA sites attached to the stiffer regions generate a higher traction force than those attached to the softer regions on a nonuniform substrate, driving the cell up the stiffness gradient.

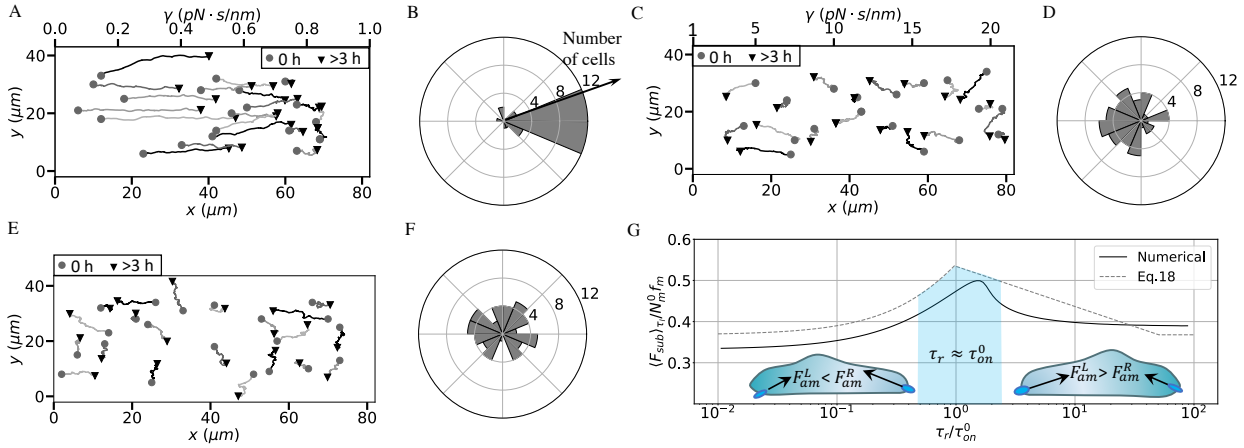

Figure 5: **Directed migration is regulated by viscosity gradient on soft substrates.** Representative trajectories of 20 cells and angular displacements of $\approx$ 50 cells on a viscoelastic substrate ($K_a = 0.1\ pN/nm$, $K_e = 2.9\ pN/nm$) with (A), (B) a linearly varying viscosity $\gamma = 0.0 - 1\ pN \cdot s/nm$, (C), (D) $\gamma = 1.0 - 20\ pN \cdot s/nm$, and (E), (F) a uniform viscosity $\gamma = 10pN \cdot s/nm$. (G) The simulated versus analytical traction forces (averaged over τ_l) as a function of the ratio of the material relaxation timescale $\tau_r \equiv \gamma/K_a$ to the clutch binding timescale $\tau_{on}^0 \equiv 1/k_{on}^0$ (Table 2). The traction forces at the two opposite ends of a cell along the direction of the motion are labeled by F_{am}^R or F_{am}^L, respectively.

We next sought to understand the impact of substrate stress relaxation on the directed migration of cells on soft substrates. In our simulations, the two stiffness values in the SLS model are set to be $K_a = 2.9\ pN/nm$ and $K_e = 0.1\ pN/nm$. We assume a nonuniform viscosity $\gamma < \gamma_0 \approx 1\ pN \cdot s/nm$ with a constant gradient $\nabla\gamma = 12.5\ pN \cdot s/\mu m^2$ in $+x-$direction, equivalent to $\tilde{\nabla}\tilde{\gamma} \approx 0.125$ in the unitless form (non-dimensionalized by γ_0 and $2r_0$). For computational efficiency, we used an $80\ \mu m \times 40\ \mu m$ domain, which is still much larger than a migrating cell size in $\pm x-$direction. The simulations demonstrate that cells migrate from the soft elastic region ($\gamma \to 0$) to the viscoelastic region, which is also evidenced by the biased angular displacement towards the $+x-$direction (Fig 5 A, B). The same trend was observed in human mesenchymal stem cells that migrate towards regions with a larger relaxation modulus on a collagen-coated polyacrylamide gel. This behavior is referred to as viscotaxis [39]. Once the substrate viscosity surpasses the threshold ($\gamma > \gamma_0$), cells migrate against the viscosity gradient with the angular displacements biased toward faster relaxation regions, which can be referred to as "anti-viscotaxis" (Fig 5 C, D). As a control, the random cell trajectories and unbiased angular displacements were observed on a uniform viscoelastic

substrate (Fig 5 E, F). These findings suggest that a viscosity gradient draws the cells to a region with $\tau_r \approx \tau_{on}^0$. The underlying mechanism for the dependence of the migration direction on the viscosity gradient can be explained by inspecting the biphasic viscosity - traction force relationship at an FA site. On soft substrates with a relaxation timescale $\tau_r < \tau_{on}^0$, an increasing viscosity contributes to an enhanced substrate traction force that counteracts retrograde actin flow. This leads to a substrate-induced polarity along the gradient. In contrast, slower relaxing substrates ($\tau_r > \tau_{on}^0$) lead to decreasing clutch lifetime (Fig I (C) in S1 Text) and the reduced mean traction forces (Eq 18). As a result, the edges of the cell attached to the faster relaxing substrate regions gain more traction, navigating the cell against the viscosity gradient (Fig 5 G).

Discussion

Our multiscale theory involves a detailed description of the adhesion reinforcement regime at each FA site and includes the cytoskeleton strain-stiffening effect, which quantitatively reproduces the large cell spreading areas on stiff substrates. Importantly, by incorporating the modified Stokes' law due to the nucleus shape change and nonlinear cytoplasmic viscosity as a function of the spreading area, we have reproduced the biphasic dependence of the migration speed on substrate stiffness. Our results demonstrate that bigger spreading areas on stiff substrates increase the cytoplasmic viscosity and flatten the nucleus, altogether increasing the drag force that in turn reduces the migration speed on stiff substrates. That way, our model reconciles the presence of the monotonic spreading area-stiffness and non-monotonic speed-stiffness relationships reported in many experiments [5, 6, 7].

Our simulations on viscoelastic substrates also reveal the influence of substrate viscosity on cell migration by tuning the engagement of the adhesion reinforcement regime. On a substrate with low instantaneous stiffness ($K_a + K_e < K_0$) where the adhesion reinforcement regime is absent, we have analytically shown the presence of a biphasic traction force-viscosity relationship at an FA site, with the traction force maximized on fast-relaxing substrates ($\tau_r \approx \tau_{on}^0$). The analytical relation helps us explain the simulation results, which quantitatively agree with the experiments. On substrates with a large instantaneous stiffness ($K_a + K_e \geq K_0$), the substrate viscosity can greatly enhance the cell spreading area due to the engagement of the adhesion reinforcement regime. Notably, although the net traction force also increases with viscosity, we observe a biphasic speed-viscosity profile with a very large additional stiffness of $K_a \gg K_0$. This is because high viscosity on a very stiff substrate triggers strong adhesion reinforcement, which induces a large

cell spreading area, in turn raising the nucleus drag force that counteracts the net traction force.

Finally, we have investigated the influence of substrate viscoelasticity on directed migration. Our model successfully captures the robust durotaxis behavior of the MDA-MB-231 cells with talin-/vinculin-mediated clutch reinforcement on elastic gradient substrates. Our simulated cells also exhibit both viscotaxis and anti-viscotaxis, with all cells migrating towards the fastest-relaxing substrate region where the traction force at an FA site is maximum when $\tau_r \approx \tau_{on}^0$. This reveals the critical role of stress relaxation in modulating the migration direction.

With these predictions and experimental validations, our theory provides a valuable tool to understand how the intricate interplay between the cellular signaling and mechanics along with cell-ECM interactions regulates migration on viscoelastic substrates. Hence, the theory paves the way for the development of novel experimental platforms for the manipulation of cell migration patterns.

Supporting Information

S1 Text. Supporting information for (A multiscale theory for spreading and migration of adhesion-reinforced mesenchymal cells). The document includes the details of implementing the adhesion reinforcement regime in the whole-cell model and the fitting of key material parameters, which are described in the Supplementary Methods section. It also contains 12 supplemental figures (Fig A-L) and 2 supplemental tables (Table A-B).

S1 Appendix. A1 - Rate coefficients in Rho GTPase reaction-diffusion model

S2 Appendix. A2 - Analytical derivation of the soft substrate force and deformation

S3 Appendix. A3 - Estimation of individual clutch force under adhesion reinforcement

Author Contributions

W.S.: conceptualization, formal analysis, investigation, software, validation, visualization, writing – original draft, review and editing; C.N.K.: conceptualization, formal analysis, project administration, resources, validation, writing – original draft, review and editing.

Declaration of Interests

The authors declare no competing interest.

Acknowledgements

We thank the College of Science at Virginia Tech for financial support.

Data availability

The source codes of the simulations can be downloaded at https://github.com/nadirkaplan/adhesion-reinforced_migration.

References

[1] Yeung T, Georges PC, Flanagan LA, Marg B, Ortiz M, Funaki M, et al. Effects of substrate stiffness on cell morphology, cytoskeletal structure, and adhesion. Cell motility and the cytoskeleton. 2005;60(1):24–34.

[2] Cheng B, Lin M, Huang G, Li Y, Ji B, Genin GM, et al. Cellular mechanosensing of the biophysical microenvironment: a review of mathematical models of biophysical regulation of cell responses. Physics of life reviews. 2017;22:88–119.

[3] Dogterom M, Koenderink GH. Actin–microtubule crosstalk in cell biology. Nature Reviews Molecular Cell Biology. 2019;20(1):38–54.

[4] Ananthakrishnan R, Ehrlicher A. The forces behind cell movement. International journal of biological sciences. 2007;3(5):303.

[5] Peyton SR, Putnam AJ. Extracellular matrix rigidity governs smooth muscle cell motility in a biphasic fashion. Journal of cellular physiology. 2005;204(1):198–209.

[6] Pathak A, Kumar S. Independent regulation of tumor cell migration by matrix stiffness and confinement. Proceedings of the National Academy of Sciences. 2012;109(26):10334–10339.

[7] Stroka KM, Aranda-Espinoza H. Neutrophils display biphasic relationship between migration and substrate stiffness. Cell motility and the cytoskeleton. 2009;66(6):328–341.

[8] Solon J, Levental I, Sengupta K, Georges PC, Janmey PA. Fibroblast adaptation and stiffness matching to soft elastic substrates. Biophysical journal. 2007;93(12):4453–4461.

[9] He S, Ji B. Mechanics of cell mechanosensing in protrusion and retraction of lamellipodium. ACS Biomaterials Science & Engineering. 2017;3(11):2943–2953.

[10] Kumar S, Maxwell IZ, Heisterkamp A, Polte TR, Lele TP, Salanga M, et al. Viscoelastic retraction of single living stress fibers and its impact on cell shape, cytoskeletal organization, and extracellular matrix mechanics. Biophysical journal. 2006;90(10):3762–3773.

[11] Bolado-Carrancio A, Rukhlenko OS, Nikonova E, Tsyganov MA, Wheeler A, Garcia-Munoz A, et al. Periodic propagating waves coordinate RhoGTPase network dynamics at the leading and trailing edges during cell migration. Elife. 2020;9:e58165.

[12] Johnson JL, Erickson JW, Cerione RA. New insights into how the Rho guanine nucleotide dissociation inhibitor regulates the interaction of Cdc42 with membranes. Journal of Biological Chemistry. 2009;284(35):23860–23871.

[13] Slaughter BD, Unruh JR, Das A, Smith SE, Rubinstein B, Li R. Non-uniform membrane diffusion enables steady-state cell polarization via vesicular trafficking. Nature communications. 2013;4(1):1380.

[14] Pathak A, Kumar S. From molecular signal activation to locomotion: an integrated, multiscale analysis of cell motility on defined matrices. PloS one. 2011;6(3):e18423.

[15] Yeoman B, Shatkin G, Beri P, Banisadr A, Katira P, Engler AJ. Adhesion strength and contractility enable metastatic cells to become adurotactic. Cell reports. 2021;34(10):108816.

[16] Isomursu A, Park KY, Hou J, Cheng B, Mathieu M, Shamsan GA, et al. Directed cell migration towards softer environments. Nature Materials. 2022; p. 1–10.

[17] Chan CE, Odde DJ. Traction dynamics of filopodia on compliant substrates. Science. 2008;322(5908):1687–1691.

[18] Bangasser BL, Rosenfeld SS, Odde DJ. Determinants of maximal force transmission in a motor-clutch model of cell traction in a compliant microenvironment. Biophysical journal. 2013;105(3):581–592.

[19] Califano JP, Reinhart-King CA. Substrate stiffness and cell area predict cellular traction stresses in single cells and cells in contact. Cellular and molecular bioengineering. 2010;3:68–75.

[20] Ghassemi S, Meacci G, Liu S, Gondarenko AA, Mathur A, Roca-Cusachs P, et al. Cells test substrate rigidity by local contractions on submicrometer pillars. Proceedings of the National Academy of Sciences. 2012;109(14):5328–5333.

[21] Elosegui-Artola A, Oria R, Chen Y, Kosmalska A, Pérez-González C, Castro N, et al. Mechanical regulation of a molecular clutch defines force transmission and transduction in response to matrix rigidity. Nature cell biology. 2016;18(5):540–548.

[22] Cheng B, Lin M, Li Y, Huang G, Yang H, Genin GM, et al. An integrated stochastic model of matrix-stiffness-dependent filopodial dynamics. Biophysical journal. 2016;111(9):2051–2061.

[23] Gong Z, Szczesny SE, Caliari SR, Charrier EE, Chaudhuri O, Cao X, et al. Matching material and cellular timescales maximizes cell spreading on viscoelastic substrates. Proceedings of the National Academy of Sciences. 2018;115(12):E2686–E2695.

[24] Elosegui-Artola A, Trepat X, Roca-Cusachs P. Control of mechanotransduction by molecular clutch dynamics. Trends in Cell Biology. 2018;28(5):356–367.

[25] Marzban B, Kang J, Li N, Sun Y, Yuan H. A contraction–reaction–diffusion model: Integrating biomechanics and biochemistry in cell migration. Extreme Mechanics Letters. 2019;32:100566.

[26] Bangasser BL, Shamsan GA, Chan CE, Opoku KN, Tüzel E, Schlichtmann BW, et al. Shifting the optimal stiffness for cell migration. Nature Communications. 2017;8(1):1–10.

[27] Adebowale K, Gong Z, Hou JC, Wisdom KM, Garbett D, Lee Hp, et al. Enhanced substrate stress relaxation promotes filopodia-mediated cell migration. Nature materials. 2021;20(9):1290–1299.

[28] Shu W, Kaplan CN. A multiscale whole-cell theory for mechanosensitive migration on viscoelastic substrates. Biophysical Journal. 2023;122(1):114–129.

[29] Lovett DB, Shekhar N, Nickerson JA, Roux KJ, Lele TP. Modulation of nuclear shape by substrate rigidity. Cellular and molecular bioengineering. 2013;6(2):230–238.

[30] Janmey PA, Fletcher DA, Reinhart-King CA. Stiffness sensing by cells. Physiological reviews. 2020;100(2):695–724.

[31] Rianna C, Radmacher M. Comparison of viscoelastic properties of cancer and normal thyroid cells on different stiffness substrates. European Biophysics Journal. 2017;46(4):309–324.

[32] Gil-Redondo JC, Weber A, Zbiral B, dM VM, Toca-Herrera JL. Substrate stiffness modulates the viscoelastic properties of MCF-7 cells. Journal of the Mechanical Behavior of Biomedical Materials. 2022;125:104979.

[33] Chaudhuri O, Cooper-White J, Janmey PA, Mooney DJ, Shenoy VB. Effects of extracellular matrix viscoelasticity on cellular behaviour. Nature. 2020;584(7822):535–546.

[34] Charrier EE, Pogoda K, Li R, Wells RG, Janmey PA. Elasticity-dependent response of malignant cells to viscous dissipation. Biomechanics and Modeling in Mechanobiology. 2021;20(1):145–154.

[35] Chaudhuri O, Gu L, Darnell M, Klumpers D, Bencherif SA, Weaver JC, et al. Substrate stress relaxation regulates cell spreading. Nature communications. 2015;6(1):1–7.

[36] Hassan AR, Biel T, Kim T. Mechanical Model for Durotactic Cell Migration. ACS biomaterials science & engineering. 2019;5(8):3954–3963.

[37] DuChez BJ, Doyle AD, Dimitriadis EK, Yamada KM. Durotaxis by human cancer cells. Biophysical journal. 2019;116(4):670–683.

[38] Shellard A, Mayor R. All roads lead to directional cell migration. Trends in cell biology. 2020;30(11):852–868.

[39] Shirke PU, Goswami H, Kumar V, Shah D, Beri S, Das S, et al. “Viscotaxis”-directed migration of mesenchymal stem cells in response to loss modulus gradient. Acta biomaterialia. 2021;135:356–367.

[40] Dokukina IV, Gracheva ME. A model of fibroblast motility on substrates with different rigidities. Biophysical journal. 2010;98(12):2794–2803.

[41] Pathak A. Modeling and predictions of biphasic mechanosensitive cell migration altered by cell-intrinsic properties and matrix confinement. Physical biology. 2018;15(6):065001.

[42] Chen PC, Feng XQ, Li B. Unified multiscale theory of cellular mechanical adaptations to substrate stiffness. Biophysical Journal. 2022;121(18):3474–3485.

[43] Chauhan BK, Lou M, Zheng Y, Lang RA. Balanced Rac1 and RhoA activities regulate cell shape and drive invagination morphogenesis in epithelia. Proceedings of the National Academy of Sciences. 2011;108(45):18289–18294.

[44] El Atat O, Fakih A, El-Sibai M. RHOG activates RAC1 through CDC42 leading to tube formation in vascular endothelial cells. Cells. 2019;8(2):171.

[45] Bangasser BL, Odde DJ. Master equation-based analysis of a motor-clutch model for cell traction force. Cellular and molecular bioengineering. 2013;6(4):449–459.

[46] De PS, De R. Stick-slip dynamics of migrating cells on viscoelastic substrates. Physical Review E. 2019;100(1):012409.

[47] Parri M, Chiarugi P. Rac and Rho GTPases in cancer cell motility control. Cell communication and signaling. 2010;8(1):1–14.

[48] Rottner K, Hall A, Small J. Interplay between Rac and Rho in the control of substrate contact dynamics. Current Biology. 1999;9(12):640–S1.

[49] Nobes CD, Hall A. Rho, rac, and cdc42 GTPases regulate the assembly of multimolecular focal complexes associated with actin stress fibers, lamellipodia, and filopodia. Cell. 1995;81(1):53–62.

[50] Zhang W, Capilnasiu A, Nordsletten D. Comparative analysis of nonlinear viscoelastic models across common biomechanical experiments. Journal of Elasticity. 2021;145(1):117–152.

[51] Bonfanti A, Kaplan JL, Charras G, Kabla A. Fractional viscoelastic models for power-law materials. Soft Matter. 2020;16(26):6002–6020.

[52] Darijani H, Naghdabadi R. Hyperelastic materials behavior modeling using consistent strain energy density functions. Acta Mechanica. 2010;213(3):235–254.

[53] Narooei K, Arman M. Generalization of exponential based hyperelastic to hyper-viscoelastic model for investigation of mechanical behavior of rate dependent materials. Journal of the mechanical behavior of biomedical materials. 2018;79:104–113.

[54] Mousavi SJ, Hamdy Doweidar M. Three-dimensional numerical model of cell morphology during migration in multi-signaling substrates. PloS one. 2015;10(3):e0122094.

[55] Loth E. Drag of non-spherical solid particles of regular and irregular shape. Powder Technology. 2008;182(3):342–353.

[56] Li Y, Lovett D, Zhang Q, Neelam S, Kuchibhotla RA, Zhu R, et al. Moving cell boundaries drive nuclear shaping during cell spreading. Biophysical journal. 2015;109(4):670–686.

[57] Wang K, Sun X, Zhang Y, Zhang T, Zheng Y, Wei Y, et al. Characterization of cytoplasmic viscosity of hundreds of single tumour cells based on micropipette aspiration. Royal Society Open Science. 2019;6(3):181707.

[58] Merchant B, Edelstein-Keshet L, Feng JJ. A Rho-GTPase based model explains spontaneous collective migration of neural crest cell clusters. Developmental biology. 2018;444:S262–S273.

[59] Zmurchok C, Holmes WR. Simple Rho GTPase dynamics generate a complex regulatory landscape associated with cell shape. Biophysical Journal. 2020;118(6):1438–1454.

[60] We converted the the experimental substrate modulus E_{sub} (kPa) to the stiffness K_{sub} (pN/nm) by using the relation $K_{sub} \approx 2E_{sub}R_{FA}$, where $2R_{FA} \approx 1.0\mu m$ approximates the diameter of the nearly circular FA region [61, 62].

[61] Horzum U, Ozdil B, Pesen-Okvur D. Step-by-step quantitative analysis of focal adhesions. MethodsX. 2014;1:56–59.

[62] Walcott S, Sun SX. A mechanical model of actin stress fiber formation and substrate elasticity sensing in adherent cells. Proceedings of the National Academy of Sciences. 2010;107(17):7757–7762.